Proceedings of ASME Turbo Expo 2020
Turbomachinery Technical Conference and Exposition
GT2020
September 21-25, 2020, Virtual, Online

GT2020-14470

ROBUST AERODYNAMIC DESIGN OF NACELLES FOR FUTURE CIVIL AERO-ENGINES

B Deneys J Schreiner
Centre for Propulsion Engineering
Cranfield University, UK
B.Deneys.J.Schreiner@cranfield.ac.uk

Fernando Tejero
Centre for Propulsion Engineering
Cranfield University, UK

David G MacManus
Centre for Propulsion Engineering
Cranfield University, UK

Christopher Sheaf
Rolls-Royce plc.
Derby, UK

ABSTRACT

As the growth of aviation continues it is necessary to minimise the impact on the environment, through reducing NO_x emissions, fuel-burn and noise. In order to achieve these goals, the next generation of Ultra-High Bypass Ratio engines are expected to increase propulsive efficiency through operating at reduced specific thrust. Consequently, there is an expected increase in fan diameter and the associated potential penalties of nacelle drag and weight. In order to ensure that these penalties do not negate the benefits obtained from the new engine cycles, it is envisaged that future civil aero-engines will be mounted in compact nacelles. While nacelle design has traditionally been tackled by multi-objective optimisation at different flight conditions within the cruise segment, it is anticipated that compact configurations will present larger sensitivity to off-design conditions. Therefore, a design method that considers the different operating conditions that are met within the full flight envelope is required for the new nacelle design challenge.

The method is employed to carry out multi-point multi-objective optimisation of axisymmetric aero-lines at different transonic and subsonic operating conditions. It considers mid-cruise conditions, end-of-cruise conditions, the sensitivity to changes in flight Mach number, windmilling conditions with a cruise engine-out case and an engine-out diversion scenario. Optimisation routines were conducted for a conventional nacelle and a future aero-engine architecture, upon which the aerodynamic trade-offs between the different flight conditions are discussed. Subsequently, the tool has been employed to identify the viable nacelle design space for future compact civil aero-engines for a range of nacelle lengths.

NOMENCLATURE

Roman Symbols

- A Area
- bc Bernstein coefficient
- C Class Function
- C_D drag coefficient
- c curve length
- D drag
- f non-dimensional parameter
- L length
- N class function exponent
- M Mach Number
- M_{is} Isentropic Mach Number
- r radius
- r_p Pearson's product-moment correlation coefficient
- r_s Spearman's rank correlation coefficient

S Shape function
v Velocity
x, y axial coordinate, ordinate

Greek Symbols

β Boat-tail angle
γ heat capacity ratio
ρ density
ψ Non-dimensional abscissa
ξ Non-dimensional ordinate

Superscripts and subscripts

cruise mid-cruise segment
diversion engine-out diversion operation
EOC end-of-cruise segment
hi highlight
if initial forebody
Mach sensitivity to increased Mach number
max maximum
nac nacelle
post post-exit
pre pre-entry
windmilling engine-out windmilling operation
∞ freestream conditions

Abbreviations

BPR bypass ratio
CFD computational fluid dynamics
DSE design space exploration
FPR fan pressure ratio
CST Class-Shape Transformation
LHS Latin Hypercube Sample
MFCR mass-flow capture ratio
SST shear-stress transport
UHBPR Ultra-High Bypass Ratio

INTRODUCTION

There is a clear need to reduce fuel-burn, perceived noise and NO_x emissions to reduce the environmental impact of aviation, while simultaneously responding to societal needs [1]. In this respect, it is expected that future civil aero-engines will operate at high bypass ratios (BPR) and low fan pressure ratios (FPR) [2] to increase the propulsive efficiency through operating at reduced specific thrust. These new architectures will have large fan diameters with associated penalties to nacelle drag, weight and installation effects [3]. The nacelle length (L_{nac}) may be shortened as much as possible to reduce the overall wetted area and nacelle drag. Consequently, this will result in a fancowl curvature reduction and a wave drag penalty [4]. Thus, for these new, challenging nacelle designs it is imperative to identify the feasible design space that does not compromise the benefits from the new engine cycles.

Typically, nacelle design was carried out by multi-point multi-objective optimisation in which different operating conditions within the cruise segment were considered. Tejero *et al.* [4] developed a nacelle design tool for axisymmetric configurations with a multi-point capability in which the mid-cruise drag, spillage drag and sensitivity to changes on flight Mach number were assessed. A set of independent multi-objective optimisation were carried out for a range of nacelle lengths and trailing edge radii. The numerical method was used to identify the feasible design space for compact future civil nacelle aero-engines and derive design guidelines. Robinson *et al.* [5] quantified the nacelle drag reduction between a conventional nacelle configuration with $L_{nac}/r_{hi} = 4.3$ and a compact architecture with $L_{nac}/r_{hi} = 3.1$ using a multi-objective design process. The proposed method resulted on a reduction of 16% on mid-cruise drag for the compact aero-engine with respect to the conventional one. Fang *et al.* [6] carried out the the nacelle design optimisation of a compact configuration with $L_{nac}/r_{hi} = 3.3$ using a tool that encompassed RANS solutions, surrogate modelling and a genetic algorithm. The design process was based on mid-cruise conditions and resulted on a optimal configuration with a 1.5 nacelle drag counts reduction with respect to a baseline design. It was also concluded that the optimisation method should consider other flight conditions to ensure robust nacelle designs. Other studies have aimed to investigate the most adequate nacelle parameterisation that covers efficiently the design space. Albert and Bestle [7] considered Class Shape Transformations (CST), superellipses and B-splines and highlighted the benefits of the CSTs over the other methods. Research has been recently extended to 3D non-axisymmetric nacelle configurations with methods based on numerical simulations and surrogate modelling [6, 8]. Nevertheless, these studies do not consider important off-design conditions during the nacelle design process.

Scope of the present work

Compact nacelle aero-engines are expected to present greater sensitivity to off-design conditions than current in-service architectures. Although for long-range applications one key consideration is the aerodynamic behaviour for cruise-type conditions, it is required to identify the feasible new nacelle design space for future civil aero-engines when off-design conditions are contemplated. This paper further develops a multi-point multi-objective optimisation tool for the aerodynamic design of nacelles.

The aim of this work is to quantify the trade-off of compact aero-engines between cruise-type and off-design conditions. The developed tool is employed to carry out independent multi-objective optimisations for a range of nacelle lengths and identify the feasible design space for the future nacelle architectures. The overall method complements a set of enabling technologies for the analysis, design and optimisation of compact nacelle archi-

tecture aiming at the reduction of specific fuel consumption.

METHODOLOGY

The nacelle design approach developed originally by Tejero *et al.* [4, 9] has been extended to account for off-design conditions. Whilst previous investigations considered mid-cruise conditions, end-of-cruise conditions and the sensitivity to changes in flight Mach number throughout the optimisation process, it is proposed to also account for windmilling conditions with a cruise engine-out case and an engine-out diversion scenario to ensure robust aerodynamic nacelle design.

The method encompasses modules for the parametric representation of the aero-engine with intuitive Class Shape Transformations, automatic structured mesh generation, a viscous compressible flow solver, a thrust-drag bookkeeping method and a evolutionary genetic algorithm. A description of the different modules is provided below.

Parametric Geometry Generation

Kulfan's Class-Shape Transformation (CST) curves [10] have been used extensively to describe aerodynamic shapes from aerofoils [11] through to complex hypersonic vehicle bodies [12]. Their application to engine design is also documented, where Albert and Bestle successfully applied CST curves to nacelle design [7]. CSTs are defined as the product of a shape function ($S(\psi)$) and a class function ($C(\psi)$) plus a vertical offset between the end points (Eq. 1):

$$\xi(\psi) = S(\psi)C(\psi) + \psi\Delta\xi_{TE};\ \xi = \frac{y}{c},\ \psi = \frac{x}{c} \tag{1}$$

where axial (x) and radial (y) are normalised by axial curve length (c). The class function, $C(\psi)$, defines the aerodynamic profile and is chosen to represent the underlying geometry. Kulfan and Bussoletti [13] proposed a class function with the form of Eq. 2:

$$C_{N2}^{N1}(\psi) = \psi^{N1}\left[1-\psi\right]^{N2} \text{ for } 0 \leq \psi \leq 1 \tag{2}$$

For given combinations of exponents (N_1, N_2), Equation 2 describes the generic profile of many common aerodynamic bodies [13], such as the Sears-Haack profile ($C_{0.75}^{0.75}$) or wedge ($C_{0.+}^{1.0}$). In the current study, a round-nose aerofoil profile is desired, which is achieved with $C_{1.0}^{0.5}$. These exponents have been commonly used to describe fan-cowl and intakes aero-engines [14].

The shape function ($S(\psi)$) is described as a series of Bernstein polynomials (Eq. 3) which result in a weighted sum of $n+1$ polynomials with the form:

$$S(\psi) = \sum_{i=0}^{n} bc_i \binom{n}{i} \psi^i (1-\psi)^{n-i} \tag{3}$$

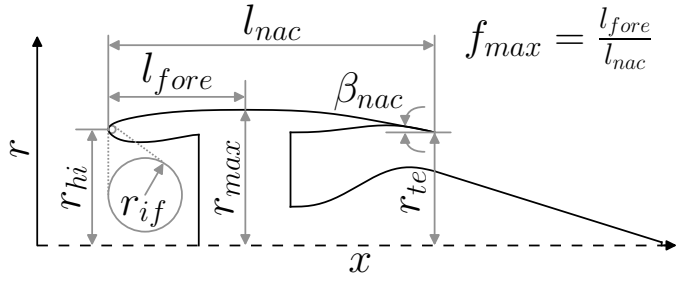

FIGURE 1. NACELLE GEOMETRY PARAMETRISATION, ADAPTED FROM [16]

where bc_i are Bernstein coefficients. For unweighted coefficients, the shape function of $n+1$ polynomials is unity. This can take any desired shape through the application of the appropriate weightings. The resulting set of $n+1$ linear equations can be solved using intuitive design variables as proposed by Zhu and Qin [15] and generalised by Christie *et al.* [14].

The proposed nacelle parameterisation uses seven intuitive variables (Figure 1) to control the fancowl aeroline. Nacelle endpoints are controlled by the highlight radius (r_{hi}), the trailing edge radius (r_{te}) and the nacelle length (L_{nac}). The nacelle CST curve is defined by the initial forebody radius (r_{if}), the maximum nacelle radius (r_{max}), the axial location of the crest (f_{max}) and the nacelle trailing edge boat-tail angle (β_{nac}). These seven nacelle design variables are used to construct a single CST curve that describes the fancowl geometry. The first ($S(0)$, Equation 4) and last ($S(1)$, Equation 5) Bernstein coefficients can be solved directly. $S(0)$ is a function of leading edge radius of curvature (eq. 4), while $S(1)$ is a function of trailing edge boat-tail angle and trailing edge ordinate (Eq. 5)

$$S(0) = bc_0 = \sqrt{\frac{2r_{if}}{c}} \tag{4}$$

$$S(1) = bc_n = \tan\beta_{nac} + \Delta\xi_{TE} \tag{5}$$

The intake and exhaust are also parametrized using intuitive design variables [14]. The framework employes a generic intake and conical exhaust to minimise the interactions with the nacelle drag characteristics. The conical exhaust afterbody is designed to produce a representative post-exit streamtube and a post-exit force term [17]. In this study, both intake and exhaust geomtries are fixed and not optimised as the framework is agnostic of engine cycle.

Computational Method

Grid generation is automated within the optimisation framework, whereby multi-block structured meshes are created in ANSYS ICEM [18] (Figure 2). The first layer height is adjusted

to satisfy a $y^+ \leq 1.0$ at all viscous wall boundaries. Grid independence was previously established for this gridding process by Heidebrecht and MacManus [17]. It reported a Grid Convergence Index (GCI) using Roache's method [19] of $GCI = 1.1\%$ for the employed mesh level of 38k cells. The farfield boundary is modeled as a semi circle, with $r_{ff} = 80r_{max}$, in accordance with previous domain sensitivities on nacelle applications [4,20]. The numerical method's accuracy was tested across Mach numbers from 0.80 and 0.89 and MFCR from 0.45 and 0.70. For cruise-type conditions with M = 0.85 and MFCR = 0.7, the nacelle drag was within 3.5% of the reported measurements. The difference between the measured and the CFD predicted drag rise Mach number is within 0.005 [21].

The compressible Navier-Stokes equations are solved using ANSYS Fluent where a second-order upwind spatial discretisation and the node Green-Gauss scheme are employed. The solver is run in density-based mode with implicit formulation and double precision. Turbulent closure for the Favre-averaged Navier Stokes equations is through Menter's [22] Shear-Stress Transport (SST) formulation of Wilcox's [23] original $k-\omega$ model. The SST formulation addresses a number of shortcomings in the original model, specifically sensitivity to freestream conditions, and improves the solution accuracy for flows with adverse pressure gradients and transonic shock waves [24]. Convergence is reached when normalised equation residuals reduce by five orders of magnitude and the oscillations in the fan cowl force over the final 500 iterations is lower than 0.05%.

Far-field free stream conditions are specified, setting static pressure, static temperature and incoming Mach number based on cruise or diversion altitude. A pressure outlet boundary is specified at the fan face, with a target mass flow set in order to achieve the desired mass-flow capture ratio (MFCR) for the engine. The fan exit is modelled through the use of a pressure inlet boundary conditions with total conditions of the far field. It aims to mimic a representative post-exit streamtube and diminish the interference effects of the nozzle on nacelle drag [21, 25]. The intake and fan-cowl are specified with no-slip walls and the nozzle walls with a slip conditions (Figure 2).

This work considers representative mid-cruise conditions of future Ultra-High Bypass Ratio (UHBPR) engines for long range applications with Mach number M = 0.85 and altitude h = 10668m. The sensitivity to changes on flight Mach number are assessed by an increment of M by 0.02 (M = 0.87) and the end-of-cruise (*EOC*) condition by a reduction of MFCR by 0.05 (MFCR = 0.65) (Table 1). Two off-design conditions are investigated to ensure robust aerodynamic nacelle design. The first scenario is an engine-out windmilling case at cruise flight Mach number, which is representative of an in-flight engine failure at altitude. The second is an engine-out diversion operation at reduced speed and altitude, typically achieved through a drift-down from cruise altitude with the remaining engine operating at maximum thrust. The diversion conditions used here are considered

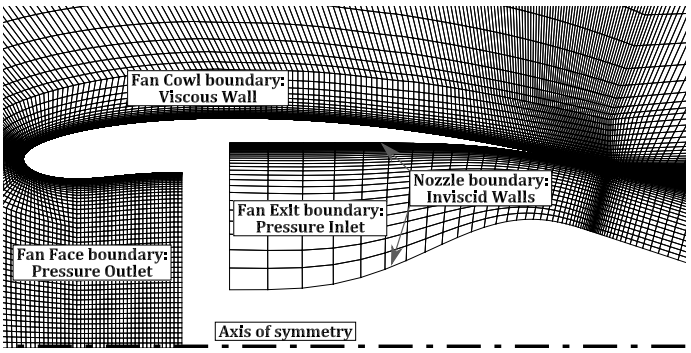

FIGURE 2. TYPICAL MESH AND BOUNDARY LOCATIONS

TABLE 1. FLIGHT CONDITIONS

Condition	Mach No.	MFCR	Altitude (m)
cruise	0.85	0.70	10668
Mach	0.87	0.70	10668
EOC	0.85	0.65	10668
windmilling	0.85	< 0.5	10668
diversion	0.65	< 0.5	< 10668

typical of a modern wide-body long-range aircraft [26] and are comparable with those for medium-range aircraft [27].

Drag Extraction

The AGARD guidelines for thrust-drag bookeeping [28] are followed in order to provide a consistent breakdown of forces. The total nacelle drag is computed from the summation of the pre-entry forces (ϕ_{pre}), the viscous and pressure forces on the nacelle (ϕ_{nac}) and the post-exit terms (ϕ_{post}) (Equation 6). These elements are visualised in Figure 3 where ϕ terms lie in the drag domain and θ terms lie in the thrust domain. Forces in the positive axial direction are taken as positive and contribute to increase drag.

$$D_{nac} = \phi_{pre} + \phi_{nac} + \phi_{post} \tag{6}$$

The modified nearfield method developed by Christie *et al.* [29] is used to calculate a combined ϕ_{pre} and ϕ_{nac}. This is achieved by integrating the momentum on the upstream infinity streamtube (F_{G0}) and on the fan face (F_{G2}), combined with force integration of pressure and viscous terms on the intake (θ_{intk}) and nacelle (ϕ_{nac}) surfaces. The ϕ_{post} term is obtained by integrating the pressures along the exit streamtube, starting at the

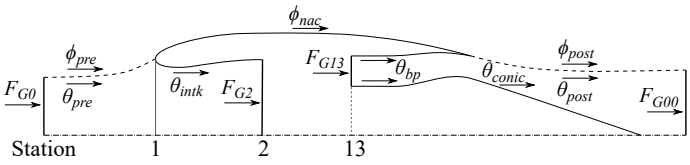

FIGURE 3. THRUST-DRAG BOOKKEEPING TERMS, ADAPTED FROM [3]

trailing edge. This exit streamtube is the boundary between drag and thrust domains. Drag is extracted during the CFD-in-the-loop operations and is passed to the optimisation routine for sorting. Results presented below are non-dimensionalised using the freestream dynamic pressure in Equation 7.

$$C_D = \frac{D}{{}^1/_2 \rho_\infty v_\infty^2 A_{hi}} \tag{7}$$

Optimisation Routine

The tool has a multi-objective optimisation capability in which the non-dominated sorting genetic algorithm (NSGA-II) has been implemented [30]. The selection of this evolutionary genetic algorithm is based on the proven suitability to identify high-dimensional Pareto fronts on non-linear data [30]. The optimisation process starts with a design of experiments from a latin hypercube sampling [31]. Subsequent generations are selected in which the nacelle drag characteristics are also evaluated with CFD. The selection of this sample size and number of generations is based on a statistical study [32] in which the sensitivity to the initial number of samples as well as total number of generations and designs per generation was assessed. It was demonstrated that the employed settings reduced the scatter on the identified Pareto front and maximised its hypervolume.

Whilst aerodynamic nacelle design optimisation has been traditionally carried out for transonic cruise-type conditions by evaluating mid-cruise ($C_{D-cruise}$), end-of-cruise (C_{D-EOC}) and sensitivity to change in flight Mach number (C_{D-Mach}), this investigation also considers two windmilling off-design conditions with a cruise engine-out case ($C_{D-windmill}$) and diversion scenario ($C_{D-diversion}$).

RESULTS AND DISCUSSION

The optimisation framework has been applied to a selection of nacelle length ratios in the range of $2.5 < L_{nac}/r_{hi} < 4.3$. A set of independent multi-point optimisations were carried out to quantify the inherent aerodynamic penalties of compact architectures under off-design operating conditions. A thorough description of the optimisation process of a conventional aero-engine architecture (L_{nac}/r_{hi} = 4.3) and a representative compact con-

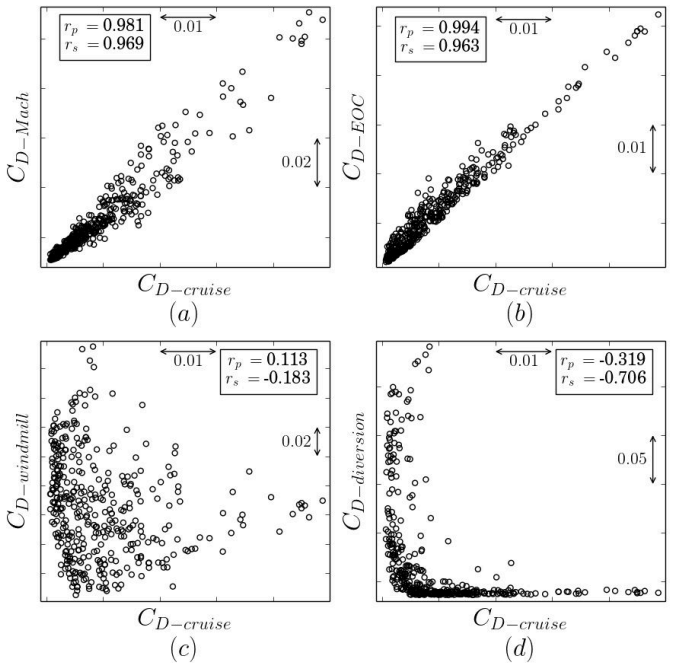

FIGURE 4. DSE FOR $L_{nac}/r_{hi} = 4.3$, ASSESSING CORRELATION OF $C_{D-cruise}$ WITH: (a) C_{D-Mach}, (b) C_{D-EOC}, (c) $C_{D-windmilling}$ and (d) $C_{D-diversion}$

figuration (L_{nac}/r_{hi} = 3.1) is presented. Subsequently, the feasible design space for future civil aero-engines when off-design conditions are considered is identified.

Conventional Design ($L_{nac}/r_{hi} = 4.3$)

Figure 4 presents the design space exploration (DSE) for the conventional nacelle length ($L_{nac}/r_{hi} = 4.3$). $C_{D-cruise}$, the primary objective function for long-range applications, is plotted against each of the remaining objective functions for the individuals in the Latin Hypercube Sample (LHS) used to explore the design space. Each frame is a two-dimensional projection of the five-dimensional space. Two correlation measures are presented. Pearson's product-moment correlation coefficient (r_p) for each function pair provides a quantitative estimate of the linear correlation. In addition, Spearman's rank correlation coefficient (r_s) is presented for each pair. This is a nonparametric measure of rank correlation between two variables, which does not assume a normal distribution of the data and assesses only the monotonicity of the relationship. Thus Spearman's rank correlation coefficient is a more appropriate measure whether a non-linear relation exists, but does not inform as to the nature of that relation. The range for this measure is $-1 \leq r_s \leq 1$, with perfect negative monotonic correlation at one extreme and perfect positive monotonic correlation at the other. $r_s = 0$ indicates no correlation.

The Pearson's product-moment of correlation (r_p) between the mid-cruise drag and the other objectives functions within the cruise segment (C_{D-EOC}, C_{D-Mach}) are both positive and close to unity (Figure 4(a) and (b)). The Spearman rank correlation complements the r_p for these traditional metrics, reinforcing that the correlation is strong and linear. As such, within an optimisation procedure the numerical assessment of one performance metric, e.g. $C_{D-cruise}$, might be sufficient to drive the genetic algorithm to the optimal part of the design space for the three performance metrics. Scatter plots between mid-cruise drag and the off-design conditions have low correlation (Figures 4(c) and (d)). For the engine-out windmilling condition ($C_{D-windmill}$) the Pearson index shows that there is no linear correlation between $C_{D-cruise}$ - $C_{D-windmill}$ and this is supported by the low r_s (Figures 4(c)). The diversion operation condition shows clustering near the axes, neither normally distributed nor linear, meaning r_p is unlikely to provide meaningful data. Indeed, this is apparent in the Spearman rank coefficient, $r_s = -0.706$, which can be understood as a strong negative correlation. This indicates that the two objectives are well posed and could form a classical front for trade-off selection.

Optimisation of the conventional ($L_{nac}/r_{hi} = 4.3$) nacelle was carried out, assessing all five objective functions. The five-dimensional Pareto front surface is projected in 2D objective space (Figure 5). Three individuals are indicated: the individual with minimum cruise drag (A1), minimum windmilling drag (A2) and a trade-off design (A3). A1 represents a design that performs exceptionally well for the three traditional measures ($C_{D-cruise}$, C_{D-Mach} and C_{D-EOC}), remaining within 2.3% of the minima for each metric (Figure 5 (a) and (b)). However, for A1 at diversion conditions, $C_{D-diversion}$ is 300% higher than the best performing individual (Figure 5 (d)). In contrast, A2 is a design selected based on $C_{D-windmilling}$ performance. At cruise, the penalty to $C_{D-cruise}$ is 20.9% (Figure 5 (a)). Under diversion conditions, a 3.1% penalty is incurred compared to the optimal $C_{D-diversion}$ individual (Figure 5 (d)). It is clear that cruise-optimum design are not suited to off-design operation. It should be noted, however, that A2 performs close to the minimum for the diversion operation. This indicates that the design challenge for conventional design has two dominant metrics, simply on- and off-design.

The trade-off design, A3, is an individual with penalties at all on- and off-design conditions: cruise performance is 6.5% worse than A1 and at windmilling there is a 40.4% increase in drag compared to A2. The engine-out diversion performance is also penalised by 36.5% compared to the $C_{D-diversion}$ minimum individual.

The changes on the nacelle drag characteristics are related to the changes on the distributions of isentropic Mach number (M_{is}, Equation 8) along the fan-cowl. For mid-cruise conditions (Figure 6 top), the A1 design experiences a strong leading-edge acceleration with the peak suction occurring almost at the

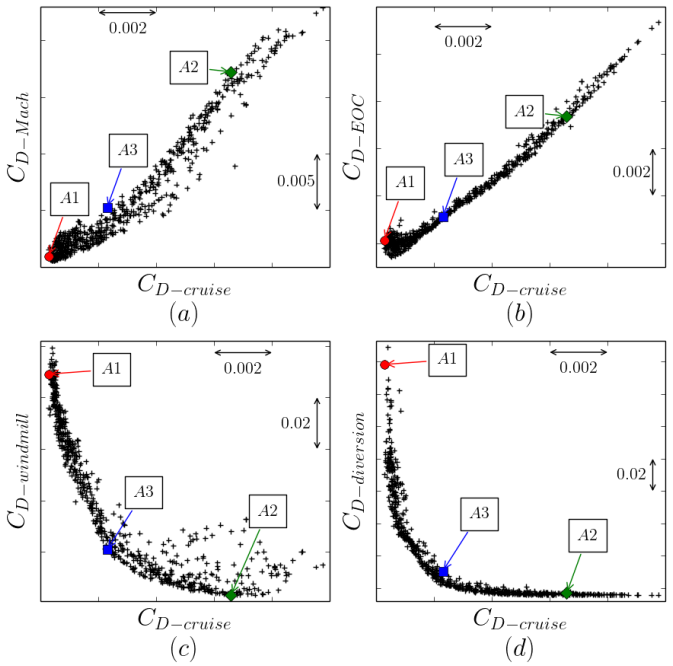

FIGURE 5. PARETO FRONT SURFACE FOR $L_{nac}/r_{hi} = 4.3$, $C_{D-cruise}$ WITH (a) C_{D-Mach}, (b) C_{D-EOC}, (c) $C_{D-windmilling}$ and (d) $C_{D-diversion}$. A1: MINIMUM $C_{D-cruise}$, A2: MINIMUM $C_{D-windmilling}$, A3: TRADE-OFF

leading edge. The flow decelerates rapidly before accelerating slightly. In comparison, A2 experiences much less severe acceleration around the leading-edge and flow continues to accelerate along the forebody. The peak M_{is} is reached near mid-cowl, after which the flow terminates to subsonic at a shock. This design is less heavily loaded over the forebody. The trade-off design, A3, shows similarity to both A1 and A2. Like A1, it experiences leading-edge acceleration that produces an initial local peak. Flow accelerates on the forebody similar to A2, reaching a peak pre-shock ahead of the mid-cowl location. This design presents a balance between the extremes at cruise. This figure also illustrates the wide range of cruise aerodynamics in the Pareto front, with the strength and location of the shock varying significantly. Figure 6 bottom presents the engine-out windmilling ($C_{D-windmilling}$) aerodynamic performance for the three selected designs. Similarities can be seen in the designs as all three experience large leading-edge accelerations with A1 reaching a prominent peak. Both A1 and A3 show flow decelerating over the forebody before terminating to subsonic at shocks at comparable non-dimensional locations. In contrast, the design A2, which has the lowest $C_{D-windmilling}$ presents a smooth deceleration along the fancowl.

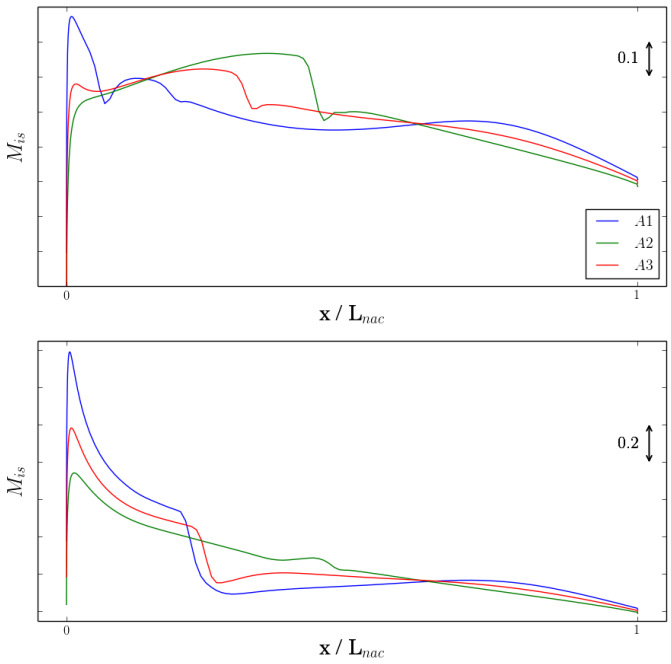

FIGURE 6. TYPICAL AERODYNAMIC PERFORMANCE FOR $L_{nac}/r_{hi} = 4.3$. TOP: CRUISE, BOTTOM: WINDMILLING

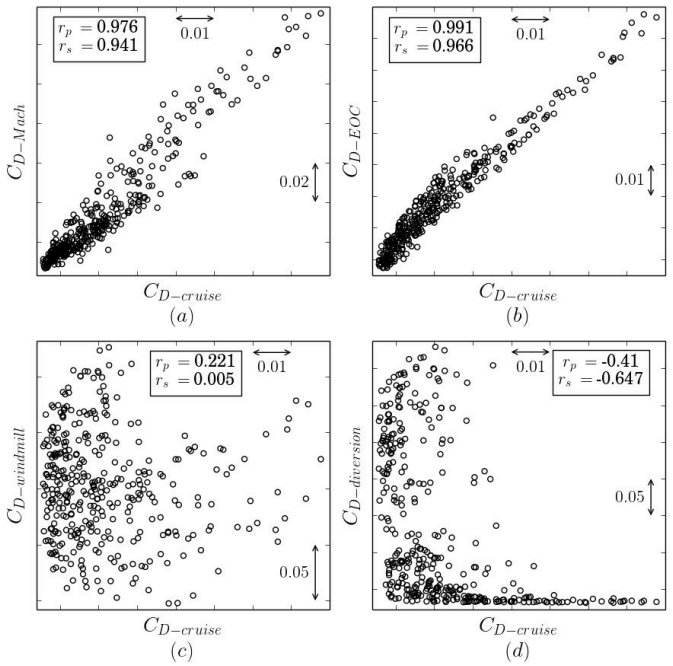

FIGURE 7. DSE FOR $L_{nac}/r_{hi} = 3.1$, ASSESSING CORRELATION OF $C_{D-cruise}$ WITH: (a) C_{D-Mach}, (b) C_{D-EOC}, (c) $C_{D-windmilling}$ and (d) $C_{D-diversion}$

$$M_{is} = \sqrt{\left[\left(\frac{P_{0\infty}}{P}\right)^{\frac{\gamma-1}{\gamma}} - 1\right]\frac{2}{\gamma-1}} \tag{8}$$

Compact Design ($L_{nac}/r_{hi} = 3.1$)

With the baseline established and the trends identified for the relatively benign configuration ($L_{nac}/r_{hi} = 4.3$), it is possible to look at the more challenging compact case of $L_{nac}/r_{hi} = 3.1$. The same metrics are applied in the same order to aid analysis. Figure 7 presents scatter plots of $C_{D-cruise}$ against each of the performance metrics for the individuals in the LHS used to explore the design space.

Here again the traditional metrics, Figure 7 (a) and (b), show positive r_p and r_s approaching unity. The correlation scores are marginally lower than their conventional counterparts indicating a deviation from linear correlation. The off-design metrics, Figure 7 (c) and (d), show a larger change. For the windmilling condition, r_s is almost exactly zero. It can be deduced that no monotonic relationship is present, compared with the small but negative value previously seen. A reduction to $r_s = -0.647$ is also indicated for the diversion condition, which can be interpreted as a moderate correlation. This would result in a Pareto front where trade-off designs can be identified.

Applying the optimisation framework to this more challenging design space obtains the Pareto fronts seen in Figure 8. The fronts are more sparsely populated than the conventional design. Again, it is possible to identify the individuals with minimum cruise drag (B1), minimum windmilling drag (B2) and a trade-off design (B3). Design B1 performs exceptionally for end-of-cruise operation (Figure 8 (b)), remaining within 1.1% of the minimum for this condition. It has degraded performance at increased Mach number (Figure 8 (a)), experiencing a 3.8% penalty compared to the minimum. The penalty at off-design conditions, however, is again large and approaches 300% in the diversion case (Figure 8 (d)). By considering these metrics against the conventional case, it could be asserted that for the on-design conditions there is no significant detriment to reducing the nacelle length. Once the off-design conditions are included, this does not hold true. For example, the best performing design during windmilling operation (B2) has a 73.7% penalty at cruise (Figure 8 (a). This design shows very high sensitivity to increased Mach number as a penalty of 194% applies compared to the minimum C_{D-Mach} individual.

The challenge of the design space is further revealed by assessing the performance of B2 at diversion (Figure 8 (d)). $C_{D-diversion}$ increases by 50.8% compared to the minimum and this design lies above the main front. This is true for almost all

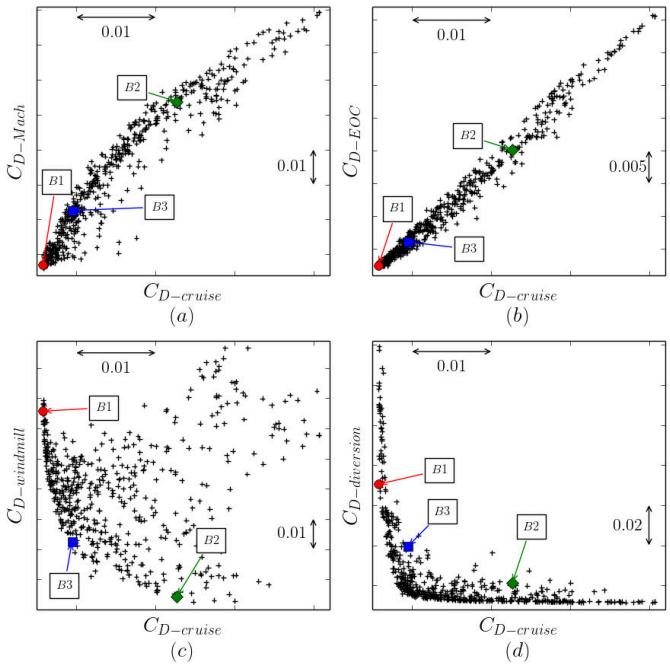

FIGURE 8. PARETO FRONT SURFACE FOR $L_{nac}/r_{hi} = 3.1$, $C_{D-cruise}$ WITH (a) C_{D-Mach}, (b) C_{D-EOC}, (c) $C_{D-windmilling}$ and (d) $C_{D-diversion}$. B1: MINIMUM $C_{D-cruise}$, B2: MINIMUM $C_{D-windmilling}$, B3: TRADE-OFF

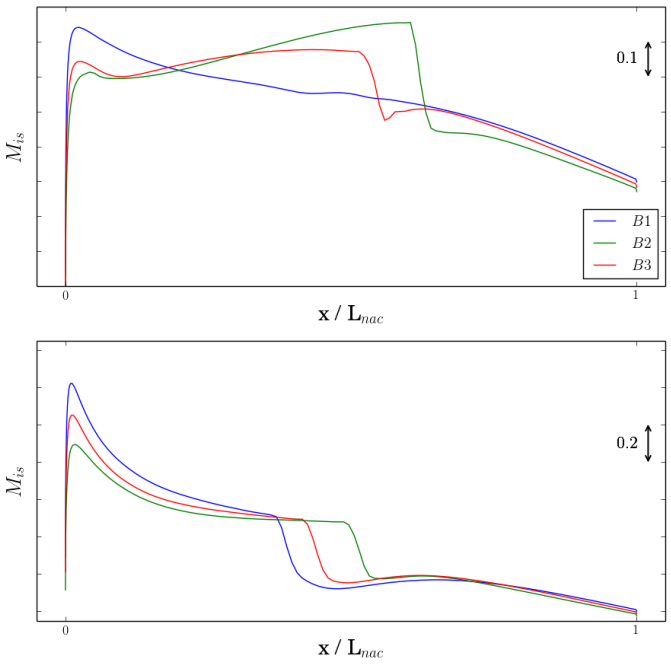

FIGURE 9. TYPICAL AERODYNAMIC PERFORMANCE FOR $L_{nac}/r_{hi} = 3.1$. TOP: CRUISE, BOTTOM: WINDMILLING

individuals with low windmilling drag and a third trade-off must be included in the selection of B3. Individual B3 performs adequately at cruise with a 14.5% penalty compared to the minimum for $C_{D-cruise}$. At end-of-cruise there a 14.1% penalty relative to the C_{D-EOC} minimum. The design is sensitive to increased Mach number, with drag increasing by 62.9% compared to the minimum for C_{D-Mach}. Windmilling performance is 38.1% worse than the minimum for $C_{D-windmilling}$, while diversion operation drag rises by 88.5% against the $C_{D-diversion}$ minimum. This compares unfavourably with the penalties incurred by A3 for the conventional design.

Of note in Figure 8 (c) is the large spread in the data. Previously (Figure 5 (c)) this spread was limited. As C_{D-Mach} and C_{D-EOC} are strongly linearly correlated with $C_{D-cruise}$, this indicating that the remaining metrics, $C_{D-windmilling}$ and $C_{D-diversion}$, are orthogonal metrics. This is not true for the compact case and is another indication of the non-linear and complex relationship between the objective functions, particularly $C_{D-windmilling}$ and $C_{D-diversion}$.

The aerodynamic performance at cruise and windmilling (Figure 9) shows similar trends to the conventional design (Figure 6). The cruise optimal design, B1, is again front loaded, but with a lower peak occurring further aft (Figure 9 top) compared to A1 (Figure 6 top). This design shows benign deceleration along the fan cowl profile. B2 experiences higher leading-edge acceleration compared to A2, exceeding the peak M_{is} value. This is followed by a slight reduction in M_{is}. The flow then accelerates, reaching a pre-shock peak M_{is} that is significantly higher than A2 before terminating at a shock to subsonic speed. The trade-off design (B3) shows similar aerodynamics to B2 and A3, but with reduced peak M_{is} and the shock location moving forward.

All three compact individuals have similar windmilling aerodynamic performance(Figure 9 bottom), also sharing similarities to A1 and A3 (Figure 6 bottom). The strong leading edge acceleration is present, thereafter the reduction in velocity is followed by a well-defined shock feature. The peak M_{is} values are reduced compared to their conventional counterparts while the shock location moves aft. In contrast to the conventional design ((Figure 6 bottom)) which show variations across the Pareto front, the aerodynamics for all three compact designs follow similar trends with large peak M_{is} and strong shockwaves near the nacelle crest.

In summary, the trade-offs for the compact design closely mirror those of the conventional design. The influence of the off-design conditions is stronger, resulting in larger penalties when against all metrics when choosing a trade-off design. This is indicative of a complex design space.

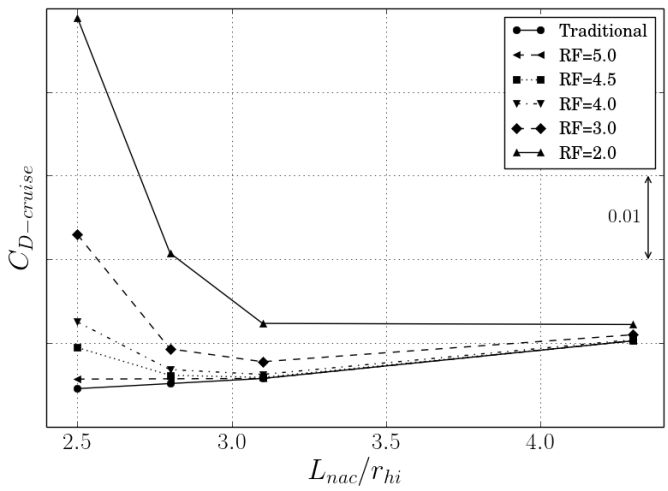

FIGURE 10. EFFECT OF ROBUST DESIGN ON CRUISE DRAG FOR SELECTED NACELLE LENGTHS

Impact of Nacelle Length on Nacelle Drag Characteristics

The influence of nacelle length on the drag characteristics across cruise as well as windmilling conditions has been studied. Independent optimisation routines were carried out for configurations with L_{nac}/r_{hi} = 2.5, 2.8, 3.1, 4.3. A set of Pareto fronts were identified upon which the trade-off between the different flight conditions can be derived. The analysis is based on the minimum achievable mid-cruise drag which fulfills that the nacelle drag at windmilling conditions ($C_{D-windmilling}$ and $C_{D-diversion}$) is below RF·$C_{D-cruise}$, where RF refers to a robustness factor. A parametric study of the influence of RF on the minimum mid-cruise for the different nacelle configurations has been performed (Figure 10). For a traditional optimisation procedure in which only cruise-type conditions are considered, the minimum $C_{D-cruise}$ reduces monotonically with nacelle length (L_{nac}/r_{hi}) across the range considered. Relative to a conventional nacelle aero-engine ($L_{nac}/r_{hi} = 4.3$), the optimisation method resulted on a reduction of 14.9 %, 17.6% and 20.4% on mid-cruise drag for the compact architectures with L_{nac}/r_{hi} = 3.1, 2.8 and 2.5, respectively. When off-design conditions, such as windmilling, are taken into account to satisfy the established RFs, other tendencies are found throughout the design space (Figure 10). For example, for a RF = 3 the expected reduction on mid-cruise drag for $L_{nac}/r_{hi} = 3.1$ is 10.4% with respect to the conventional architecture, the $L_{nac}/r_{hi} = 2.5$ presents a penalty of 38.6%. The results highlight the non-linear changes in performance that future compact civil aero-engines may present when considering these off-design conditions.

CONCLUSIONS

A framework for the multi-point optimisation of axisymmetric nacelle aerolines has been further developed to include off-design conditions and the conical nozzle. The tool incorporates geometry definition using intuitive Class-Shape transformations, a mesh generation capability, an automated CFD process, a thrust-drag bookkeeping procedure and the NSGA-II genetic algorithm. The method has been employed to carry out several multi-objective optimisations, in which different flight conditions that are met throughout the flight envelope were considered. Whilst nacelle design has been traditionally tackled by considering conditions within the cruise segment, the proposed method also evaluates different windmilling scenarios to ensure the robustness of the nacelle aerodynamic design.

A set of independent optimisation routines were carried out to identify the feasible design space for compact future civil aero-engines. When considering only traditional cruise segment criteria, it is possible to reduce $C_{D-cruise}$ by 20.4% when shortening the nacelle from $L_{nac}/r_{hi} = 4.3$ to 2.5. It has been demonstrated that the inclusion of off-design conditions during the design process can lead to different optimal parts of the design space. This is caused by the high non-linearity of the associated transonic flow aerodynamics on compact nacelle aero-engines at windmilling conditions. As such, for this new nacelle design challenge it is required to consider off-design conditions to ensure robust nacelle designs. For RF = 3, the benefit of the $L_{nac}/r_{hi} = 2.5$ nacelle is negated, while the $L_{nac}/r_{hi} = 3.1$ nacelle provides a $C_{D-cruise}$ improvement of 10.4% . The presented results demonstrate that the proposed tool is an enabling technology for the design and optimisation of future civil aero-engines which aim for the reduction of aircraft fuel burn.

ACKNOWLEDGMENT

This project has received funding from the Clean Sky 2 Joint Undertaking under the European Union's Horizon 2020 Research and Innovation Program under Grant Agreement No 820997.

References

[1] Birch, N., 2000. "2020 Vision: The Prospects for Large Civil Aircraft Propulsion". *The Aeronautical Journal,* ***104***(1038), pp. 347–352.

[2] Guha, A., 2011. "Optimum Fan Pressure Ratio for Bypass Engines with Separate or Mixed Exhaust Streams". *Journal of Propulsion and Power,* ***17***(5), pp. 1117–1122. DOI: 10.2514/2.5852.

[3] Tejero, F., Goulos, I., MacManus, D., and Sheaf, C., 2020. "Effects of Aircraft Integration on Compact Nacelle Aerodynamics". In AIAA SciTech Forum and Exposition, AIAA Paper 2020-2225. DOI: 10.2514/6.2020-2225.

[4] Tejero, F., Robinson, M., MacManus, D. G., and Sheaf, C., 2019. "Multi-objective optimisation of short nacelles for high bypass ratio". *Aerospace Science and Technology,* ***91***, pp. 410–421. DOI: 10.1016/j.ast.2019.02.014.

[5] Robinson, M., MacManus, D., Richards, K., and Sheaf, C., 2017. "Short and Slim Nacelle Design for Ultra-High BPR Engines". In 55th AIAA Aerospace Sciences Meeting, AiAA SciTech Forum. AIAA 2017-0707, DOI: 10.2514/6.2017-0707.

[6] Fang, X., Zhang, Y., Li, S., , and Chen, H., 2016. "Transonic Nacelle Aerodynamic Optimization Based on Hybrid Genetic Algorithm". In 17th AIAA/ISSMO Multidisciplinary Analysis and Optimization Conference. AIAA 2016-3833, DOI: 10.2514/6.2016-3833.

[7] Albert, M., and Bestle, D., 2013. "Aerodynamic Design Optimization of Nacelle and Intake". In *Proceedings of ASME Turbo Expo 2013: Turbine Technical Conference and Exposition*. San Antonio, TX, June 3-7, 2013. GT2013-94857, DOI: 10.1115/GT2013-94857.

[8] Zhong, Y., and Li, S., 2017. "A 3D Shape Design and Optimization Method for Natural Laminar Flow Nacelle". In Proceedings of ASME Turbo Expo 2017: Turbomachinery Technical Conference and Exposition. GT2017-64379, DOI: 10.1115/GT2017-64379.

[9] Tejero, F., MacManus, D. G., and Sheaf, C., 2019. "Surrogate-based aerodynamic optimisation of compact nacelle aero-engines". *Aerospace Science and Technology,* ***93***. DOI: 10.1016/j.ast.2019.05.059.

[10] Kulfan, B. M., 2010. "Recent extensions and applications of the 'CST' universal parametric geometry representation method". *The Aeronautical Journal,* ***114***(1153), pp. 157–176. DOI: 10.1017/S0001924000003614.

[11] Sripawadkul, V., Padulo, M., and Guenov, M., 2010. "A Comparison of Airfoil Shape Parameterization Techniques for Early Design Optimization". In 13th AIAA/ISSMO Multidisciplinary Analysis and Optimization Conference. AIAA 2010-9050, DOI: 10.2514/6.2010-9050.

[12] Liu, C., Duan, Y., Cai, J., and Wang, J., 2016. "Application of the 3D multi-block CST method to hypersonic aircraft optimization". *Aerospace Science and Technology,* ***50***, pp. 295 – 303. DOI: 10.1016/j.ast.2015.06.019.

[13] Kulfan, B. M., and Bussoletti, J. E., 2006. ""Fundamental" Parametric Geometry Representations for Aircraft Component Shapes". In 11th AIAA/ISSMO Multidisciplinary Analysis and Optimization Conference. AIAA 2006-6948, DOI: 10.2514/6.2006-6948.

[14] Christie, R., Heidebrecht, A., and MacManus, D. G., 2017. "An Automated Approach to Nacelle Parameterization Using Intuitive Class Shape Transformation Curves". *Journal of Engineering for Gas Turbines and Power,* ***139***(6), pp. 062601–1 – 9. DOI: 10.1115/1.4035283.

[15] Zhu, F., and Qin, N., 2014. "Intuitive Class/Shape Function Parameterization for Airfoils". *AIAA Journal,* ***52***(1), pp. 17–25. DOI: 10.2514/1.J052610.

[16] Christie, R., Robinson, M., Tejero, F., and MacManus, D. G., 2019. "The use of hybrid intuitive class shape transformation curves in aerodynamic design". *Aerospace Science and Technology*, p. In Press. DOI: 10.1016/j.ast.2019.105473.

[17] Heidebrecht, A., and MacManus, D. G., 2019. "Surrogate model of complex non-linear data for preliminary nacelle design". *Aerospace Science and Technology,* ***84***, pp. 399 – 411. DOI: 10.1016/j.ast.2018.08.020.

[18] ANSYS ®. *Academic Research, Release 18.2, Help System, ICEM*. ANSYS, Inc.

[19] Roache, P., 1994. "A Method for Uniform Reporting of Grid Refinement Studies". *Journal of Fluids Engineering,* ***116***(3), pp. 405–413. DOI: 10.1115/1.2910291.

[20] Heidebrecht, A., Stańkowski, T. P., and MacManus, D. G., 2016. "Parametric Geometry and CFD Process for Turbofan Nacelles". In Proceedings of ASME Turbo Expo 2016: Turbomachinery Technical Conference and Exposition, ASME. GT2016-57784, DOI: 10.1115/GT2016-57784.

[21] Robinson, M., MacManus, D. G., and Sheaf, C., 2019. "Aspects of aero-engine nacelle drag". *Proceedings of the Institution of Mechanical Engineers, Part G: Journal of Aerospace Engineering,* ***233***(5), pp. 1667–1682. DOI: 10.1177/0954410018765574.

[22] Menter, F. R., 1994. "Two-Equation Eddy-Viscosity Turbulence Models for Engineering Applications". *AIAA Journal,* ***32***(8), pp. 1598–1605. DOI: 10.2514/3.12149.

[23] Wilcox, D. C., 1998. *Turbulence Modelling for CFD*, 1st ed. DCW Industries, La Canada.

[24] ANSYS ®. *Academic Research, Release 18.2, Help System, Fluent*. ANSYS, Inc.

[25] Tejero, F., MacManus, D., and Sheaf, C., 2020. "Impact of Droop and Scarf on the Aerodynamic Performance of Compact Aero-Engine Nacelles". In AIAA SciTech Forum and Exposition, AIAA Paper 2020-1522. DOI: 10.2514/6.2020-1522.

[26] Robinson, M. H., 2018. "The Aerodynamics of Aero-Engine Nacelles". PhD Thesis, Cranfield University, Cranfield, UK.

[27] Bode, C., Friedrichs, J., Somdalen, R., Köhler, J., Büchter, K.-D., Falter, C., Kling, U., Ziolkowski, P., Zabrocki, K.,

Müller, E., and Kožulović, D., 2017. "Potential of Future Thermoelectric Energy Recuperation for Aviation". *Journal of Engineering for Gas Turbines and Power,* ***139***(10). DOI: 10.1115/1.4036527.

[28] MIDAP Study Group, 1979. Guide to In-Flight Thrust Measurement of Turbojets and Fan Engines. Tech. Rep. AGARDograph No. 237, AGARD.

[29] Christie, R., Ramirez, S., and MacManus, D. G., 2014. "Aero-engine installation modelling and the impact on overall flight performance". In Advanced Aero Concepts, Design and Operations Conference, Royal Aeronautical Society.

[30] Deb, K., Pratap, A., Agarwal, S., and Meyarivan, T., 2002. "A Fast and Elitist Multiobjective Genetic Algorithm: NSGA-II". *IEEE Transactions on Evolutionary Computation,* ***6***(2), April, pp. 182 – 197. DOI: 10.1109/4235.996017.

[31] Helton, J. C., and Davis, F. J., 2003. "Latin hypercube sampling and the propagation of uncertainty in analyses of complex systems". *Reliability Engineering and System Safety,* ***81***(1), pp. 23–69. DOI: 10.1016/S0951-8320(03)00058-9.

[32] Robinson, M. H., MacManus, D. G., Heidebrecht, A., and Grech, N., 2017. "An Optimisation Method for Nacelle Design". In 55th AIAA Aerospace Sciences Meeting, AiAA SciTech Forum. AIAA 2017-0708, DOI: 10.2514/6.2017-0708.